

# Contact-mediated nucleation in melt emulsions investigated by rheo-nuclear magnetic resonance

Gina Kaysan<sup>1</sup>  | Nicolas Schork<sup>2</sup>  | Sabrina Herberger<sup>1</sup> |  
Gisela Guthausen<sup>2,3</sup>  | Matthias Kind<sup>1</sup> 

<sup>1</sup>Institute for Thermal Process Engineering, KIT, Karlsruhe, Germany

<sup>2</sup>Institute for Mechanical Engineering and Mechanics, KIT, Karlsruhe, Germany

<sup>3</sup>Engler-Bunte Institute, Water Science and Technology, KIT, Karlsruhe, Germany

## Correspondence

Matthias Kind, Institute for Thermal Process Engineering, KIT, 76131 Karlsruhe, Germany.  
Email: matthias.kind@kit.edu

## Funding information

Deutsche Forschungsgemeinschaft, Karlsruher Institut für Technologie

## Abstract

Increasing the efficiency of disperse phase crystallization is of great interest for melt emulsion production as the fraction of solidified droplets determines product quality and stability. Nucleation events must appear within every single one of the  $\mu\text{m}$ -sized droplets for solidification. Therefore, primary crystallization requires high subcooling and is, thus, time and energy consuming. Contact-mediated nucleation is a mechanism for intensifying the crystallization process. It is defined as the successful nucleation of a subcooled liquid droplet induced by contact with an already crystallized droplet. We investigated contact-mediated nucleation under shear flow conditions up to shear rates of  $457 \text{ s}^{-1}$  for a quantitative assessment of this mechanism. Rheo-nuclear magnetic resonance was successfully used for the time-resolved determination of the solids fraction of the dispersed phase of melt emulsions upon contact-mediated nucleation events. The measurements were carried out in a dedicated Taylor–Couette cell. The efficiency of contact-mediated nucleation  $\lambda_{\text{sec}}$  decreased with increasing shear rate, whereas the effective second order kinetic constant  $k_{\text{coll,eff}}$  increased approximately linearly at small shear rates and showed a linear decrease for shear rates higher than about  $200 \text{ s}^{-1}$ . These findings are in accordance with coalescence theory. Thus, the nucleation rate is optimal at specific flow conditions. There are limitations for successful inoculation at a low shear rate because of rare contact events and at a high shear rate due to too short contact time.

## KEYWORDS

<sup>1</sup>H-NMR, contact-mediated nucleation, droplet crystallization, melt emulsion, Rheo-NMR, secondary nucleation

## 1 | INTRODUCTION

Emulsions are thermodynamically instable mixtures of two rather immiscible liquids. Emulsions with crystalline disperse phases, called melt emulsions, play a major role in fields of food technology, life science, and pharmaceutical research. Current research focuses on knowledge-based control of the stability of melt emulsions during storage and transportation. Accordingly, incomplete droplet crystallization must be efficiently mitigated. Secondary contact-mediated nucleation must be considered for increasing the fraction of solidified droplets (i.e., particles) during production processes. It is understood as nucleation upon collision of subcooled liquid droplets with particles. A quantitative understanding of this mechanism is still lacking and, hence, is the focus of this study. Compared with primary nucleation, contact-mediated nucleation occurs at lower subcooling, where subcooling is defined as the temperature difference between melting point temperature and sample temperature.

Droplets that either collide with each other or with particles can coalesce, aggregate, or separate from each other again after the collision (e.g., Chesters<sup>[1]</sup>). According to Dickinson et al.,<sup>[2]</sup> one out of  $10^7$  collisions of a particle with a subcooled droplet leads to droplet crystallization in a quiescent n-hexadecane-in-water emulsion (Sauter diameter  $x_{3,2} = 0.32 - 0.37 \mu\text{m}$ ). The collision of two droplets or a droplet and a particle can be triggered by random particle motion (Brownian motion, perikinetic), externally applied velocity fields (orthokinetic), and velocity differences due to density and size differences in the gravitational field.<sup>[3]</sup> The collision rate results as a superposition of these effects. Different densities, droplet sizes and swarm effects in real melt emulsions add complexity. However, perikinetic effects generally become less important for particle sizes above one micrometer compared to orthokinetic collision.<sup>[4]</sup> Moreover, no droplet deformation occurs during the experiments as the maximal Capillary number is  $\ll 0.1$  and the ratio between disperse and continuous dynamic viscosity is calculated as 3.<sup>[5,6]</sup> Thus, the extensional flow should not lead to an enhancement of collision incidence.

One possibility to expose emulsions to different but defined shear rates is the use of the Taylor–Couette geometry. Flow between two concentric, moving cylinders has been under investigation since the 17th century.<sup>[7]</sup> The patterns of flow in a Taylor–Couette reactor (TCR) are well described in literature (e.g., Andereck et al.<sup>[8]</sup>), some of them were determined by magnetic resonance imaging (MRI) (e.g., Seymour et al.<sup>[9]</sup>). In contrast to a stirred tank, the TCR geometry offers the

advantage that a narrow distribution of the shear rate is ensured, and influences from fluid dynamic on the process can be studied more precisely. Another positive aspect is the high ratio between heat exchange surface and reaction volume, which enables isothermal experiments.

As will be shown later, the combination of a TCR with the capabilities of nuclear magnetic resonance (NMR) has a great potential for investigating the influence of shear flow on crystallization. This combination is described in literature as one realization of Rheo-NMR and has been used to study the flow behavior of and in complex fluids.<sup>[10–22]</sup> Moreover, a concentration gradient of the disperse phase of an emulsion in a shear field was observed.<sup>[23]</sup> In addition, shear-induced migration of oil droplets within a Taylor–Couette geometry was described,<sup>[24]</sup> whereas highly concentrated adhesive emulsions showed only a small radial dependence of the droplet volume fraction.<sup>[25]</sup> Furthermore, recrystallization and network formation of crystalline dispersions of a fat were successfully investigated.<sup>[26,27]</sup> Rheo-NMR also allowed the exploration of the influence of fluid dynamics on polymerization as a function of temperature.<sup>[28]</sup>

In a preliminary study,<sup>[29]</sup> the crystallization of emulsions was inline measured by NMR at a laminar Couette flow. A self-made setup according to Morimoto et al.<sup>[21]</sup> was used with a rotating outer cylinder. The shear rate in the experiments carried out by Kaysan et al.<sup>[29]</sup> was limited to about  $300 \text{ s}^{-1}$ , and only laminar Couette flow could be realized. Nevertheless, the setup ensured stable and reproducible flow conditions at an exactly defined temperature and a well-defined flow field.<sup>[29]</sup> These experiences lead to the current study at technically relevant shear rates.

According to Smoluchowski,<sup>[30]</sup> the collision kernel for laminar flow  $\beta_{SL,lam} [\text{m}^3 \text{ s}^{-1}]$  is calculated as a function of shear rate  $\dot{\gamma} [\text{s}^{-1}]$ , while  $x_1 [\text{m}]$  and  $x_2 [\text{m}]$  represent the droplet sizes of the colliding partners:

$$\beta_{SL,lam} = \frac{4}{3} \dot{\gamma} \left( \frac{x_1}{2} + \frac{x_2}{2} \right)^3. \quad (1)$$

Analogous to the coalescence theory of droplets, it can be assumed that not all collisions of subcooled droplets with already solidified droplets lead to nucleation. It is well known that the coalescence process can be divided into three successive steps. At first, the two droplets approach each other. This may have different causes, such as perikinetic or orthokinetic movement. The following, second step is the film drainage. The film thickness between the two interfaces must be below a critical

value for coalescence to take place.<sup>[31]</sup> The film drainage depends strongly on the difference between buoyancy and gravity, the interfacial tension, and the material system properties. It is considered as the time-determining step for coalescence.<sup>[32]</sup> Moreover, the surfactants at the interface play a major role as they influence the coalescence time greatly (e.g., other studies<sup>[33–35]</sup>). This is due to the impact of surfactant on circulation flows in the droplets and on flows at the phase boundary due to local concentration differences (Marangoni effect) (e.g., Hodgson et al.<sup>[36,37]</sup>). The last third step is the film rupture. Beginning at a distance of about 100 nm, additional forces, such as the attractive Van der Waals forces and repulsive electrostatic or oscillatory forces, due to the appearance of either surfactant at the interfaces or micelles in the continuous phase are in play.<sup>[38–40]</sup> In addition to the collision frequency, the time that two colliding droplets are in contact with each other is crucial.

The nucleation efficiency  $\lambda_{sec}$  [–] is introduced to quantify the crystallization efficiency.<sup>[29]</sup> If all collisions led to crystallization, the nucleation efficiency would be 1.

$$\lambda_{sec} = \frac{k_{coll,eff}}{\beta_{SL} n_{total}}, \quad (2)$$

where  $k_{coll,eff}$  [ $s^{-1}$ ] is an effective second order constant, describing the reaction rate constant of contact-mediated nucleation.  $n_{total}$  [ $m^{-3}$ ] represents the number density of all liquid droplets  $n_L$  [ $m^{-3}$ ] and solid particles and, because the disperse phase is constant during the experiments,  $n_{total} = n_L(t_0)$ .  $t_0$  is the time before starting subcooling, that is, all droplets are in liquid state.

The fraction of crystallized droplets  $\xi(t)$  [–] at a time  $t$  [s] can be quantified by a second order kinetics (e.g., Dickinson et al.<sup>[2,41]</sup>):

$$\frac{d(1-\xi)}{dt} = -k_{coll,eff} \xi(1-\xi). \quad (3)$$

Once crystallization occurs due to a reactive collision, the newly formed particles are assumed to cause nucleation with the same reactivity as the initial solid particles.

The validity of this approach of contact-mediated nucleation will be proven for the solidification kinetics of the disperse phase of melt emulsions. A link can be made between coalescence processes and contact-mediated nucleation.

## 2 | RESULTS AND DISCUSSION

### 2.1 | Flow fields in the Rheo-NMR device

The flow field in the gap was measured via MRI as it provides a basis for data interpretation to determine crystallization efficiency.

To calculate the theoretical mean magnitude velocity  $u_{xy,mag,mean}$ , the surface velocity of the inner cylinder was defined as the maximum velocity and the assumption was made that the velocity drops off completely across the gap as evidenced by the MRI data. A no-slip condition, a thin gap and Newtonian flow behavior were assumed as the disperse volume fraction is 20 wt-%.<sup>[18]</sup> Moreover, we observed the Newtonian behavior of the emulsion during rheological measurements.

To determine the mean magnitude velocity experimentally, MR images of the TCR gap filled with liquid emulsion ( $\Delta T_{sub} = 2.5$  K [ $\pm 0.5$  K], no crystallization) were segmented into concentric rings. The calculated magnitude velocities,  $u_{xy,mag}(x,y)$ , in each one pixel-wide ring were averaged over the angle to obtain  $u_{xy,mag}$  as a function of the radius, using similar data quantification as that described in refs.<sup>[42,43]</sup> (Figure 1a). This procedure leads to a good numerical stability of the velocity data up to 5 Hz. Any angular dependence of  $u_{xy,mag}(r)$  was excluded by inspecting the MRI images beforehand.  $u_{xy,mag}(r)$  represents the magnitude velocity at a radial position  $r$ , not to be confounded with the velocity component along a constant radius. The mean magnitude velocity  $u_{xy,mag,mean}$  was then calculated by volume-averaging all velocities in the gap (Figure 1b).

Figure 1b indicates that the experimental data have a maximum deviation of 15% compared with the theoretically calculated mean magnitude velocities. The deviation increases with the increasing rotation speed, which is either due to the use of the ring method in averaging the experimental data, due to fluctuations in the speed of rotation, or due to the assumptions used for the theoretical calculation (e.g., linear profile across the gap). There is no clear evidence for wall slip at higher rotational speeds as with increasing shear rate, wobbling, that is, weak movements of the inner cylinder in the guidance, can occur. These movements influence data acquisition as well as data processing via the ring method but also limit the matching of the theoretical expectation and experimental observation. Consequently, measurement errors have to be considered as well as the complexity of the emulsion's rheologic behavior, which does not allow postulations about wall slip. As the experiments were carried out with liquid emulsion at a subcooling where no primary crystallization took place, any influences of the

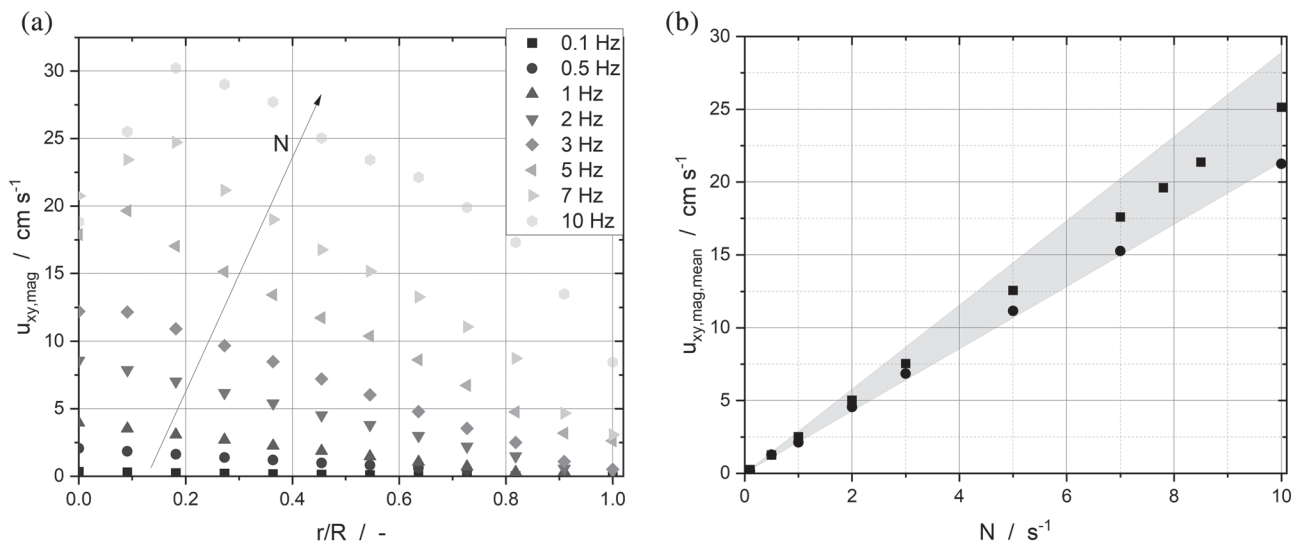


**FIGURE 1** (a) Velocity profiles across the gap  $r/R$  filled with the liquid emulsion at different rotational velocities. (b) Mean magnitude velocity  $u_{xy,mag,mean}$  from theoretical calculations (squares) and experimentally determined mean magnitude velocities (circles) as a function of revolution rate  $N$ . The gray area corresponds to an error of 15%. The theoretical values were calculated by linear interpolation of the circumferential velocity of the inner cylinder to the velocity at the outer cylinder ( $u_{xy,mag,mean} = 0$ )

viscosity can be neglected during one experiment at a constant shear rate. For shear rates between 0.2 and  $500 \text{ s}^{-1}$  a constant dynamic viscosity of  $2 \cdot 10^{-3} \text{ Pa s}$  was measured for the liquid emulsion. Therefore, viscosity of the liquid emulsion should not change throughout the experiments.

Nevertheless, the linear velocity profiles were observed very clearly (Figure 1a), and the experimental and theoretical results show good agreement ensuring a well-defined and well-known flow field. Moreover, the onset of a nonlinear profile at 10 Hz may result from the changing flow profile from the laminar Couette flow to the laminar Taylor eddy flow. We were not able to detect any Taylor eddies by measuring  $u_z$  because the velocity determination at a speed of 10 Hz turned out to be complex in spite of triggering.

Hanlon et al.<sup>[44,45]</sup> showed a linear velocity profile for a Newtonian fluid under laminar Couette flow. Additionally, Gottwald et al.<sup>[46]</sup> and Callaghan et al.<sup>[12]</sup> measured a linear velocity profile for laminar Couette flow and, thereby, showed the application of NMR and MRI to determine flow profiles in small gaps. Gabriele et al.<sup>[47]</sup> showed no wall-slip for dairy emulsions. Furthermore, they measured an increase of nonlinearity of the velocity profile along the gap with higher shear rates. A nonlinear shear profile across the gap was also measured for worm-like micelle systems due to the appearance of shear banding independent of the shear rate.<sup>[48–50]</sup> Taylor vortex flow was measured by MRI by, for example, Seymour et al.<sup>[9]</sup> and Vallatos et al.<sup>[51]</sup> These findings are in good

agreement with our results, although we could not detect any Taylor eddies at 10 Hz.

Shear rates  $\dot{\gamma}(r)$  were calculated according to<sup>[18]</sup>

$$\dot{\gamma}(r) = r \frac{\partial \left( \frac{u_{xy,mag}(r)}{r} \right)}{\partial r}. \quad (4)$$

As velocity linearly varies in the gap for  $N < 10 \text{ Hz}$ , the shear rate shows no radial dependence. Only one value defines the shear per rotation speed.

Different characteristic numbers are known in literature to describe flow within the TCR. Reynolds numbers, for example, are used to describe the flow regimes. The Reynolds number for TCR was calculated as

$$Re_{TCR} = \frac{u_{xy,mag,mean} \cdot s}{\nu}, \quad (5)$$

where  $\nu$  [ $\text{m}^2 \text{ s}^{-1}$ ] represents the kinematic viscosity of the emulsion, determined by rheological measurements as  $2.0 \cdot 10^{-6} \text{ m}^2 \text{ s}^{-1}$ , and  $s$  [m] represents the gap width.

The critical Reynolds number ( $Re_{crit}$ ) describes the transition of the laminar Couette flow to the laminar Taylor eddy flow. Further critical Reynolds numbers are defined for the transition from eddy flow to wave flow ( $Re'_{crit} = 1.05 - 10 \cdot Re_{crit}$ ), depending on the cylinders' size and the gap width.<sup>[52–54]</sup> Moreover, flow maps enable the approximation of the flow regime by taking the geometry and the angular velocity into consideration.<sup>[8]</sup>

$Re_{crit}$  was calculated for the transition from the laminar Couette to the laminar Taylor eddy flow by Equation 6 according to Esser and Grossmann<sup>[55]</sup>:

$$Re_{crit} = \frac{1}{0.1556^2} \cdot \frac{(1+\eta)^2}{2\eta \cdot \sqrt{(1-\eta)(3+\eta)}}, \quad (6)$$

where  $\eta$  hereby denotes the ratio between the radii of the inner and the outer cylinder ( $\eta = r_i / (r_i + s)$ ). For the actual experimental setup  $Re_{crit} = 121$ , which corresponds to a rotation frequency of the inner cylinder of 8.8 Hz. The critical Reynolds number for the transition to laminar vortices only depends on  $\eta$  which can be justified by the aspect ratio  $\Gamma$  (quotient of cylinder length and gap width). According to Cole,<sup>[54]</sup> for example, this is guaranteed for  $\Gamma > 40$ . In the setup shown here,  $\Gamma$  is 77, which justifies the use of Equation 6.

## 2.2 | Experimental results

The fraction of n-hexadecane droplets which were solidified due to secondary contact-mediated nucleation  $\xi_{sec,hex}$  was measured as a function of time  $t$  (Figure 2a).  $\xi_{sec,hex}(t)$  was found to also depend on  $N$  and, hence, on  $\dot{\gamma}_{mean}$ . The approximation in Equation 3 was used to determine the effective collision's kinetic factor  $k_{coll,eff}$  (Figure 2b). All data sets were smoothed via a moving average over five points.

The effective kinetic parameter  $k_{coll,eff}$  has been analyzed as a function of  $\dot{\gamma}_{mean}$  (Figure 3a) according to Equations 1 and 2.

$k_{coll,eff}$  strongly depends on  $\dot{\gamma}_{mean}$  (Figure 3a). It increases approximately linearly with  $\dot{\gamma}_{mean}$  up to  $\dot{\gamma}_{mean} \sim 150 \text{ s}^{-1}$ , whereas a linear decrease has been detected for  $\dot{\gamma}_{mean} > 150 \text{ s}^{-1}$ . Also, the nucleation efficiency of these secondary nucleation events,  $\lambda_{sec}$ , strongly depends on  $\dot{\gamma}_{mean}$  (Figure 3b).

Different aspects of contact crystallization of emulsions have been described in literature. A distinction can be made between investigations with superposition of primary and secondary nucleation under flow,<sup>[56,57]</sup> only secondary nucleation in flow fields,<sup>[29,58]</sup> and secondary nucleation without external flow (only Brownian motion).<sup>[2,59,60]</sup>

Mudge and Mazzanti<sup>[61]</sup> noticed that higher shear rates did not necessarily result in higher solid fat contents of cacao butter but they can also hinder crystallization. The latter is also seen in the results presented here, as the total solid fraction increases up to about 29% at a rotational frequency of 3 Hz and then decreases as a function of mean shear rate. Mazzanti et al.<sup>[62]</sup> showed that the shear-induced crystallization depends on the fraction of canola stearin which was mixed with canola oil: Hardly any triggering of crystallization by external stress was detected for canola stearin fractions of 20% and 40%.

A linear correlation between  $k_{coll,eff}$  and  $\dot{\gamma}_{mean}$  was also found for laminar Couette flow up to shear rates of

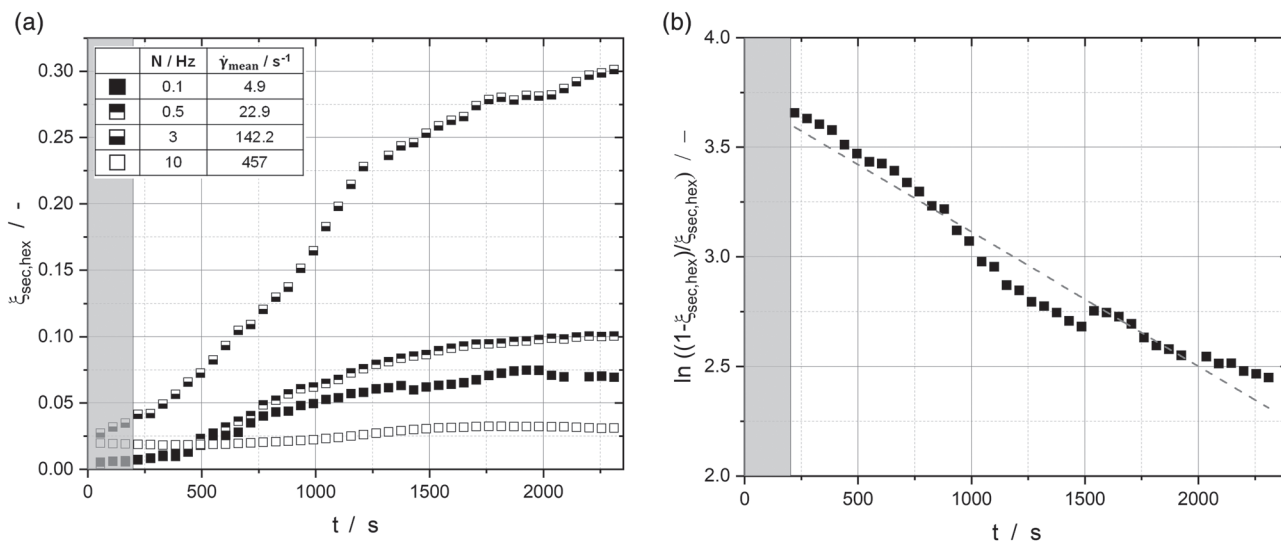


**FIGURE 2** (a) Fraction of n-hexadecane droplets solidified due to secondary nucleation as a function of time  $t$ , starting when temperature reached  $15.5^\circ\text{C}$  ( $\Delta T = 2.5 \text{ K}$ ).  $^1\text{H}$  spectra were measured during shearing of the emulsion at four different  $\dot{\gamma}_{mean}$ . The fraction of solid seeds produced by primary nucleation was about 10% to 15% (not shown for better clarity). (b) Exemplarily for a rotational frequency of 0.1 Hz; Equation 3 is shown to overall describe the data well (gray line) after the differential equation was solved (see supporting information). The gray areas in (a) and (b) represent the waiting time where temperature equilibrium had not yet been reached

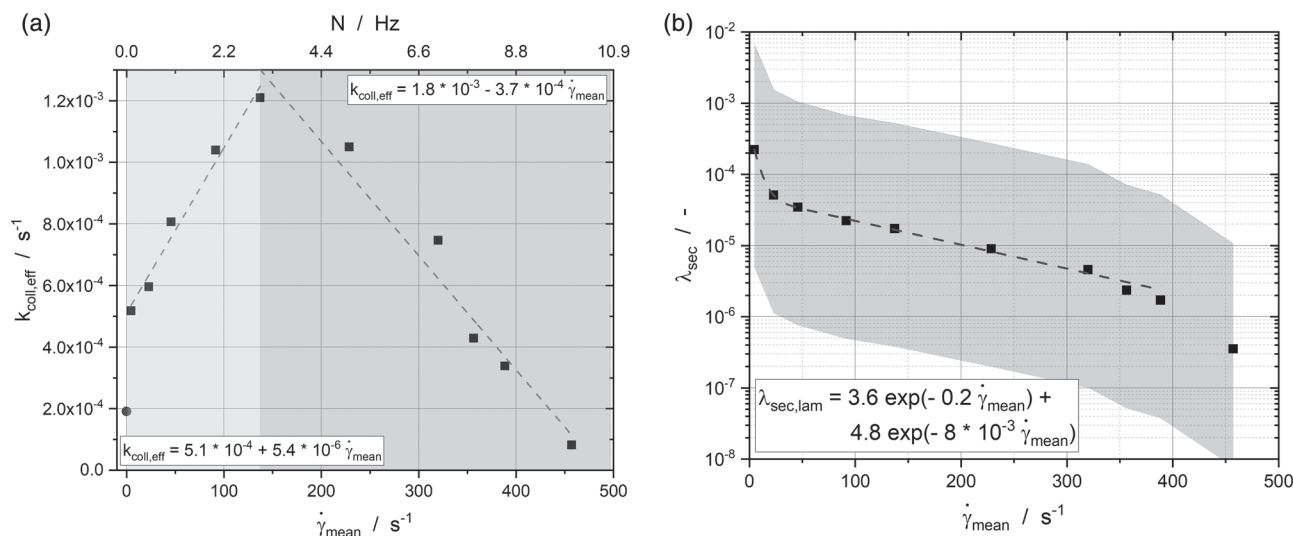


**FIGURE 3** (a) Second order kinetic constant  $k_{coll,eff}$  as a function of mean shear rate  $\dot{\gamma}_{mean}$ . Two areas are visible reflecting two dominating factors (collision frequency and contact time). The dashed lines represent linear fits to the data. (b) Nucleation efficiency  $\lambda_{sec}(\dot{\gamma}_{mean})$  for the emulsion with  $x_{50,3} = 2.8 \mu\text{m}$  (black squares),  $\sigma = 1.2 \mu\text{m}$ , and span  $0.9$  to  $10.2 \mu\text{m}$ . A biexponential fit describes the secondary nucleation efficiency for laminar flow  $\lambda_{sec,lam}$ . The biexponential fit is an empirical description of the experimental data. The nucleation efficiency at  $10$  Hz ( $\dot{\gamma}_{mean} = 457 \text{ s}^{-1}$ ) is not considered for the fit as the flow regime changed at  $8.8$  Hz

$296 \text{ s}^{-1}$ .<sup>[29]</sup> One collision out of  $3 \cdot 10^5$  resulted in the nucleation of a liquid droplet by a crystallized particle. Dickinson et al.<sup>[2]</sup> reported one out of  $10^7$  collisions leading to nucleation. The experiments presented here are between  $1.5 \cdot 10^2$  and  $1.3 \cdot 10^8$ , depending on the collisions' partners' sizes and mean shear rate, where smaller shear rates and, thus, smaller relative velocities and smaller droplet sizes led to higher contact-mediated nucleation efficiency.

Because there are some similarities between coalescence and contact-mediated crystallization, an explanation of the results obtained is given here only based on the coalescence theory. Within this concept, the assumption is made that the distance between the subcooled droplet and the crystalline particle must fall below the critical film thickness for nucleation.<sup>[31]</sup> There are two main differences between coalescence and contact nucleation: (1) The phase boundary of the liquid droplet can be either mobile or immobile, whereas the phase boundary of the crystallized droplet is assumed to be constantly immobile. (2) When droplets approach particles, the phase boundary of the liquid droplet can deform, whereas the phase boundary of the crystallized droplet is considered to be nondeformable.

Three models are known to describe the collision efficiency  $\lambda$ <sup>[31]</sup>: Two physical approaches (the energy model<sup>[63–65]</sup> and film drainage model (e.g., other studies<sup>[1,66–69]</sup>) and one empirical (the critical velocity model<sup>[70,71]</sup>). By transferring these approaches to contact-mediated nucleation, the energy model would suggest

nucleation for relative velocities higher than a critical relative velocity. This approach cannot explain the decrease of secondary nucleation efficiency  $\lambda_{sec}$  with increasing flow velocities. The critical velocity model takes the observations of Doubliez<sup>[72]</sup> and Duineveld<sup>[73]</sup> into account, presenting a dependence on contact force. Thus, contact-mediated nucleation should be sensitive to the strength of collisions, favoring the gentle ones. Using the critical velocity approach, the data obtained, especially at  $\dot{\gamma}_{mean} > 200 \text{ s}^{-1}$ , can be explained by higher forces at higher shear rates and, thus, lower nucleation efficiencies.

The film drainage model uses the contact time and the drainage time to determine the efficiency, while the drainage time is proportional to the contact force.<sup>[1,68,74]</sup> Levich<sup>[4]</sup> and Chesters<sup>[1]</sup> described an inversely proportional behavior between contact time and energy dissipation for turbulent flow. Krebs et al.<sup>[75]</sup> and Zhou et al.<sup>[76]</sup> found higher contact times at lower, laminar flow velocities in microfluidic setups. With higher flow velocities, the contact force (and, thus, the drainage time) increases, whereas the contact time decreases. Both results would lead to lower collision efficiencies, which is in good agreement with the results presented here. The biexponential decay in Figure 3b) is motivated by the exponential dependence of the efficiency from drainage and contact time.

Considering these findings, the maximum of  $k_{coll,eff}$  appearing as a function of  $\dot{\gamma}_{mean}$  should result from higher collision numbers and, thus, higher solid

fractions, as long as there is no limitation due to the contact time. Further investigations are planned which elucidate this interplay of the influencing factors, collision strength, collision time and collision number.

### 3 | CONCLUSION

Contact-mediated nucleation of a model melt emulsion was investigated by Rheo-MRI up to shear rates of  $457 \text{ s}^{-1}$  at a rotational speed of 10 Hz. An increasing crystal content of the disperse phase could be determined up to shear rates of about  $150 \text{ s}^{-1}$ . The final solid contents decreased within the same time intervals when further increasing shear rates. However, as the nucleation efficiency is additionally considered, it decreases with the shear rate for all flow velocities. Therefore, the impact of contact time, which is inversely proportional to the shear rate, and the increasing number of possible collisions can be pointed out very clearly and for the first time within one geometry. Using the same geometry is important to ensure small shear rate distributions and, thus, comparable results. Transferring these results to industrial emulsion production, higher solid contents may be reached by combining primary and secondary nucleation mechanisms at gentle stirring.

A TCR was developed and established to perform these MRI experiments. The imprinted channels ensured homogeneous and rapid sample temperature equilibration and control. The flow velocities determined by MRI showed a maximum deviation of 15% to the theoretically calculated flow velocities.

Further investigations to finally clarify the triggering effect of contact-mediated nucleation in industrial processes are planned in a laboratory stirred tank to also take transient and turbulent flow fields into consideration. Very wide velocity and shear rate distributions are present during industrial emulsion production. According to the results presented here, the highest nucleation efficiencies and solid fractions of dispersed phases are expected at low stirring rates. This would enable a more energy and cost-effective production, which means better sustainability in melt emulsion production.

MRI method developments have the perspective to gain more insight into shear-induced crystallization. Questions arise how pulse sequences and post processing can be further tailored to fit the needs and conditions of the TCR. Additionally, diffusion allows to measure droplet size distributions spatially resolved. Changes thereof could be detected as a function of shear rate. A use of the inverse Abel or Hankel transformation for the

cylindrically symmetric object such as the TCR could be further explored, for example, Douglass et al.<sup>[77]</sup>

## 4 | EXPERIMENTAL

In the following, the production of the investigated melt emulsions is described. Moreover, the methodology based on NMR for measuring the transient behavior of the fraction of solidified droplets upon well-controlled fluid dynamic conditions in a TCR is summarized.

### 4.1 | Melt emulsion

Regarding the preparation of a 50-ml stock of the model emulsion, 20 wt-% n-hexadecane as the disperse phase ( $\text{C}_{16}\text{H}_{34}$ , Hexadecane ReagentPlus<sup>®</sup>, Sigma-Aldrich<sup>®</sup>, purity: 99%, melting temperature  $18^\circ\text{C}$ ), 2 wt-% polysorbate 20 (Tween<sup>®</sup>20, Merck<sup>®</sup> KGaA) as surfactant and 78 wt-%  $\text{D}_2\text{O}$  (Deutero<sup>®</sup>, purity: 99.9%) were emulsified at room temperature for 5 min at 20,000 rpm in a gear rim dispersing machine (IKA<sup>®</sup> T25 digital). A fresh stock was prepared every week to avoid long-term effects, such as coalescence or agglomeration. Measurements of the droplet size distributions were done with a Mastersizer 3000E (Malvern Panalytical GmbH). The volumetric mean droplet diameter of the stock emulsion was modeled with a logarithmic normal distribution (droplet mean diameter  $x_{50,3} = 2.8 \mu\text{m}$ , width of the distribution  $\sigma = 1.2 \mu\text{m}$ , span 0.9 to  $10.2 \mu\text{m}$ ). The stock was manually shaken carefully before taking samples for guaranteeing reproducibility.

### 4.2 | Viscosity measurements

The viscosity of the emulsion was measured in triple determination at  $20^\circ\text{C}$  on a Physica MCR 301 rheometer (Anton Paar, Germany). A double-slit geometry DG 26.7 was used with a slit width of 2 mm and a cylinder height of 40 mm.

### 4.3 | Experimental setup: Rheo-NMR cell

The experiments were carried out in a Taylor–Couette Rheo-NMR cell (Figure 4). It comprises a rotating inner cylinder, which is connected to a shaft and driven by an external motor from the top. This inner cylinder is placed into the stationary outer cylinder and the gap is formed in which the fluid (emulsion) is exposed to well-defined

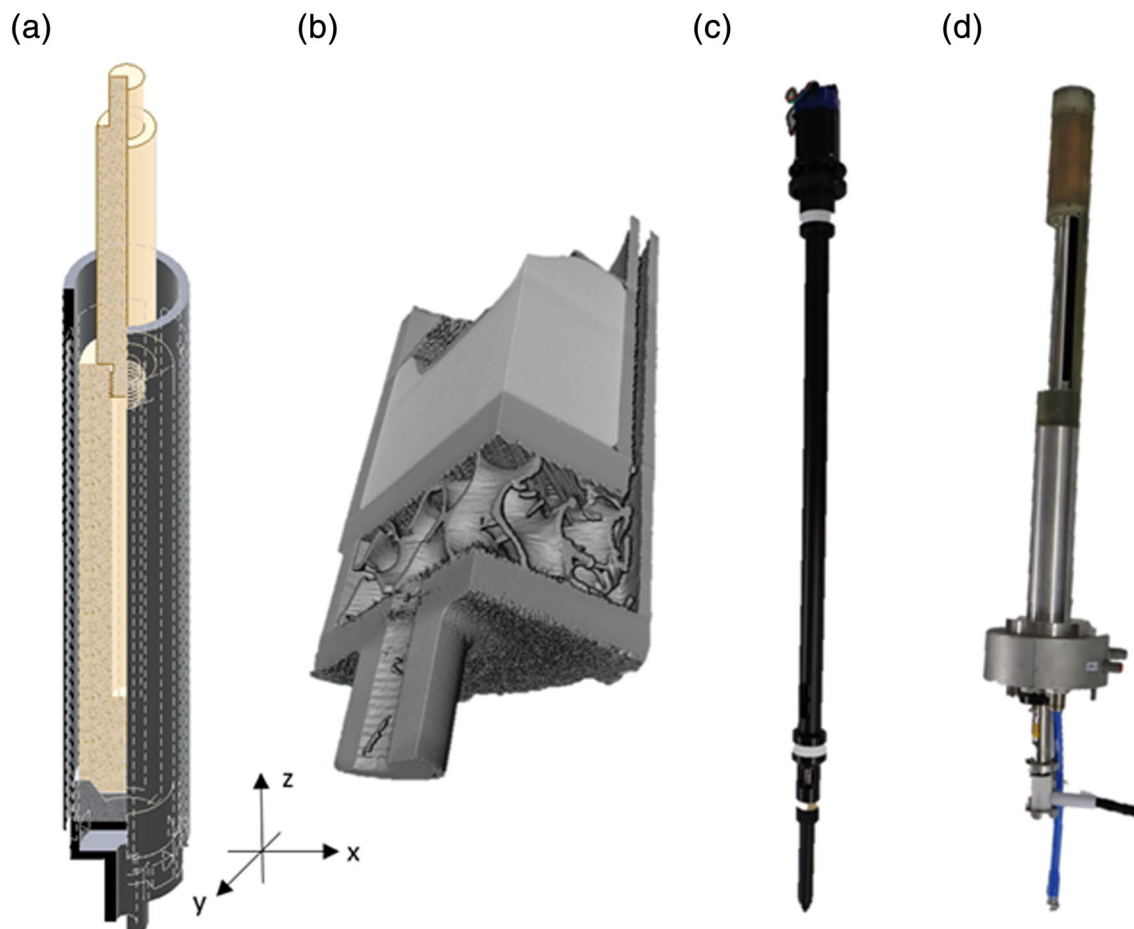


**FIGURE 4** (a) Three-dimensional (3D) sketch of the Taylor–Couette Rheo-nuclear magnetic resonance (NMR) cell (see supporting information for a detailed technical drawing). The part in dark gray is the outer cylinder of the Taylor–Couette reactor. It comprises channels for temperature control by thermostated  $N_2$ . The light gray component at the bottom of the dark gray cylinder is the guidance for the inner cylinder and is manufactured from polyether ether ketone. The rotating inner cylinder is also made of polyether ether ketone and is shown in beige. It has a cavity in its center, which is filled with methanol for in situ temperature measurement. Please also note the coordinate system, which will be used throughout this publication. (b)  $\mu$ CT 3D image of the outer cylinder and the guidance for the inner cylinder (light gray). The gas inlet at the bottom and its distribution through the outer wall of the cells are shown in detail. (c) Upper part of the Rheo-NMR setup of Bruker, including the motor, drive shaft, and coupling to which the inner cylinder is connected. (d) Bottom part of the measurement setup, including the temperature sensor and the temperature control of gas cooling or heating. In the present experiments, cooled nitrogen gas was transported to the Rheo-NMR cell inside a glass dewar. The setup was inserted into a Bruker probe of the MICWB 40 series with a 25-mm birdcage resonator

shear stress. The outer cylinder is part of a more complex bottom piece and is held by a support rod from the bottom. The inner cylinder is centered regarding the outer cylinder by a dedicated guidance piece. A similar realization of a TCR, also with a tempering capability, was constructed in Wageningen.<sup>[22]</sup>

The bottom piece of the cell is 3D printed and made from GreenTEC (FD3D GmbH). This material is a mixture of a polylactic acid copolyester and additives. The thermophysical data used for the estimation of temperature homogeneity are given in Table 1. All other components were manufactured from polyether ether ketone (Eisen-Schmitt, Germany). The inner diameter of the

**TABLE 1** Summary of the relevant substance properties of GreenTEC at  $15.5^\circ\text{C}$  used for determining the time required for temperature equilibration

Parameter	Value
Density	$1.22 \text{ g cm}^{-3}$
Heat capacity	$1.324 \text{ J g}^{-1} \text{ K}^{-1}$
Thermal conductivity	$0.251 \text{ W m}^{-1} \text{ K}^{-1}$

outer cylinder is 18.2 mm. Gas channels in the wall of the outer cylinder provide the possibility to regulate temperature in the sample volume. The wall thickness

between the gap and the channels was 0.6 mm. The outer diameter of the inner cylinder was 16 mm, resulting in a gap width of 1.1 mm. The Rheo-NMR cell is connected to a dedicated Rheo-NMR setup (Bruker Biospin, Germany). This setup consists of a bottom and a top part and allows for rotational speeds of up to 10 Hz.

The inner cylinder has a central cavity filled with methanol (Merck, Darmstadt, Germany), which allows in situ temperature measurements. The difference in the chemical shift of the two methanol peaks ( $-\text{OH}$  and  $\text{CH}_3$ ) was quantified to provide an NMR thermometer.<sup>[78]</sup> The data of the external temperature sensor are compared with the temperature of the methanol inside the inner cylinder during the experiments and are kept constant. This provides a temperature control of the sample within  $\pm 0.5$  K.

#### 4.4 | NMR settings for characterization of the Rheo-NMR cell and measurement of the crystallization

The temporal development of the fraction of solidified droplets upon various flow conditions has been measured by Rheo-NMR. The Taylor–Couette cell was designed for such measurements in the super wide bore magnet of a 200 MHz HDIII spectrometer (MICWB 40 series, Bruker Biospin, Germany) equipped with a 25-mm birdcage resonator (Figure 4d). Due to the super wide bore of the magnet and the radial extension of the TCR, the spectral resolution is limited when compared with a liquid-state NMR spectrometer, but the larger dimension allows investigations of a significant thermostated volume of sample.

Furthermore, not only the structural dimensions of the cell can be measured in MRI but also the velocity field. Regarding structural dimensions, it is a prerequisite for meaningful experiments regarding flow, chemical composition, and crystallization that the geometry of the inner and outer cylinders is exact, within  $\pm 5\%$ . This prerequisite was checked before starting the experiments and could be proven by structural MRI.

Phase-contrast MRI in a gradient echo-based pulse sequence (FLOWMAP) was used to measure the velocity field (Table 2, Figure 5a). Consequently, the velocity in all three spatial dimensions was measured, well knowing that some deviations of the measurement from the real flow field were described in literature due to the implementation of the pulse sequence in Paravision 6.0.1.<sup>[22]</sup> Two subsequent measurements with different flow gradients  $G_{\text{flow}}$  ( $G_{\text{flow},1} \neq G_{\text{flow},2}$ ) are analyzed in terms of phase differences  $\Delta\Phi$  to measure the phase difference.  $\Delta\Phi$  is then converted into a velocity for each voxel and

TABLE 2 Magnetic resonance imaging (MRI) parameters for the measurement of flow velocity

MRI parameter	Value
Pulse sequence	FLOWMAP
$T_R$	0.5 s
$\tau_E$	5 ms
Number of averages	8
Slice thickness (z-direction)	3 mm
Number of slices	1
Flip angle	60°
Field of view (x-, y-direction)	20 mm $\times$ 20 mm
Matrix size (x-, y-direction)	256 $\times$ 256
Measurement duration	34 min 8 s

velocity direction. The maximum measurable absolute velocity in an experiment, also known as the “field of flow,” must be adjusted for every single rotational speed. The TCR has small inaccuracies in the 3D-printed housing in the form of vibrations and motions, for example, resulting from the backlash of the coupling. As a result, deviations may occur in the form of motion effects, which result in an imaging artefact. This motion-related phase artefact can be reduced by triggering the MRI experiment to a certain position of the inner cylinder of the TCR, that is, by synchronizing motor position and MRI experiment.

The velocity field in x-, y-, and z-direction ( $u_{x,y,z}$ ) was measured in an axial slice at  $z = 2.5$  cm above the bottom of the gap volume in three separate 2D spatially resolved MRI measurements. Next, the magnitude of both transverse velocities,  $u_{xy,mag} = \sqrt{u_x^2 + u_y^2}$ , was calculated.  $u_z$  was measured and checked to exclude eddies or flow irregularities. Only very small velocities in the z-direction were measured ( $u_z/u_{xy,mag} < 0.01$ ) for all rotational speeds as expected. Because  $u_z$  is much smaller than  $u_{xy,mag}$ ,  $u_z$  will not be considered in the following.

The spectral information was measured in an axial slice also at  $z = 2.5$  cm by applying a spin echo-based chemical shift imaging experiment to obtain spatially resolved information about the fraction of solidified droplets. A two-dimensional chemical shift imaging experiment was modified to allow for a one-dimensional measurement (Table 3, Figure 5b). The motivation was the following: Compared with 2D phase-encoding, measurement time is significantly reduced, because only one instead of two phase-encoding gradients must be incremented to measure the spatially resolved spectral information. On the other hand, the measurement time of one chemical shift imaging experiment must be sufficiently small when compared with the overall nucleation

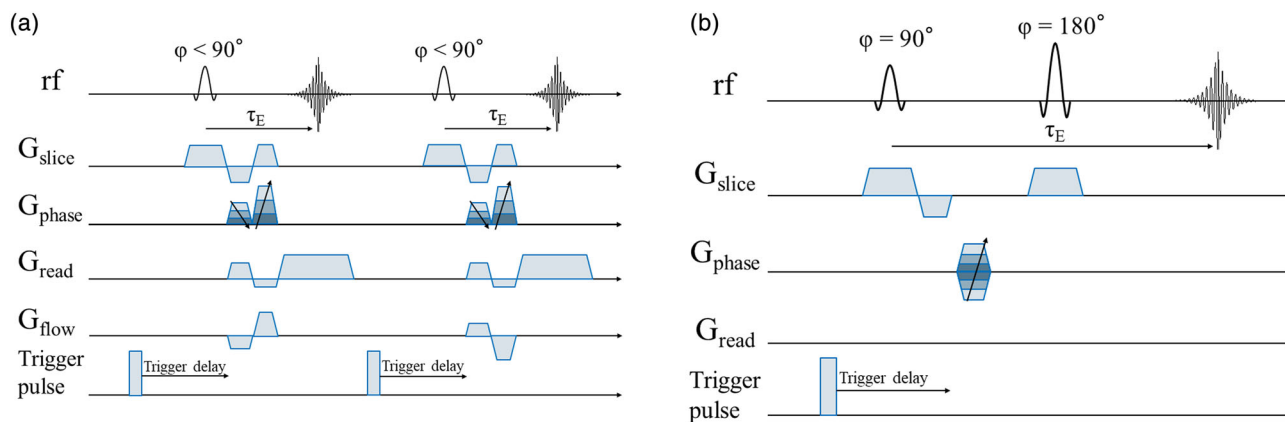


**FIGURE 5** (a) Method for measuring the velocity field  $u_{x,y,z}$  in the gap of the Taylor–Couette reactor (TCR) by a gradient echo-based pulse sequence (FLOWMAP) in axial slices ( $xy$ ) by setting the direction and amplitudes of  $G_{\text{flow}}$  accordingly. Synchronization between the TCR and magnetic resonance imaging (MRI) is achieved by a trigger pulse of the Rheo interface. (b) A slice-selective spin echo-based chemical shift imaging pulse sequence was used to measure the chemical composition in the axial slices. A trigger pulse from the Rheo interface again allows for artefact reduction by triggering the MRI measurement on the phase encoding step

**TABLE 3** Magnetic resonance imaging (MRI) parameters for the measurement of spectral information during the rotation of the inner cylinder of the Taylor–Couette reactor (TCR)

MRI parameter	Value
Pulse sequence	1D SE-CSI
$T_R$	2 s
$\tau_E$	3 ms
Number of averages	4
Slice thickness ( $z$ -direction)	3 mm
Number of slices	1
Field of view ( $x$ -direction)	20 mm
Matrix size ( $x$ -direction)	8
Spectral band width (SWH)	5 kHz
Number of acquired data points	2048
Number of dummy scans	4
Measurement duration	42 s

process to provide sufficient time-resolution of the measurements. At the same time, the spectral information is influenced by the fast rotational motion ( $N > 1$  Hz) of the inner cylinder and the geometry of the whole TCR setup, which is influenced by magnetic field inhomogeneities. Thus, a 1D-CSI experiment resulted in the best compromise of fast spatially resolved measurements and good spectral information during rotational motion of the TCR. Practically, eight phase-encoding steps were measured along  $x$ ; the information in the  $y$ -direction was summed up, resulting in eight projections along  $y$  as a function of  $x$ . A neglect of one dimension is acceptable to obtain the spectral information over the entire Couette gap, which is independent on the angle. Line broadening

due to fast rotation of the inner cylinder of the TCR is small, and the approach allows a good quantification of the spectra (see Figure 7). All eight spectra were quantified regarding their signal-to-noise, line broadening and similarity. As a result, it was found that only the two spectra at the edges of the cell deviated significantly from the others. Without loss of information, only the fourth spectrum (middle) was used for all subsequent calculations.

#### 4.5 | Rheo-NMR measurement on melt emulsions

Before starting an experiment, the gap of the TCR was externally filled with 5-ml n-hexadecane-in-water emulsion. The loaded TCR then was connected to the upper part of the Rheo-NMR setup of Bruker (Figure 4c) and integrated into the spectrometer. To guarantee the temperature control, the bottom part of the measurement setup (Figure 4d) was finally coupled from below to study the contact-mediated nucleation at a well-defined subcooling. At the beginning of each experiment, an emulsion with a 10 to 15 wt-% fraction of solidified n-hexadecane droplets was prepared by primary crystallization at a subcooling of  $\Delta T_{\text{sub}} = 14$  K. Thereafter, the subcooling was reduced to  $\Delta T_{\text{sub}} = 2.5$  K ( $\pm 0.5$  K) within the metastable range and kept constant throughout the rest of the experiment. At this reduced subcooling temperature, no further primary crystallization took place, and solid particles did not thaw. After the signal intensity became constant, the experiment began by starting the rotation. The experiment lasted 40 min. The complete time scheme is schematically shown in Figure 6.

**FIGURE 6** Schematic temperature profile used for all experiments. The gray area represents the metastable zone where no primary nucleation would occur, and the reddish range shows the time at constant temperature and rotational speed where contact-mediated nucleation was measured

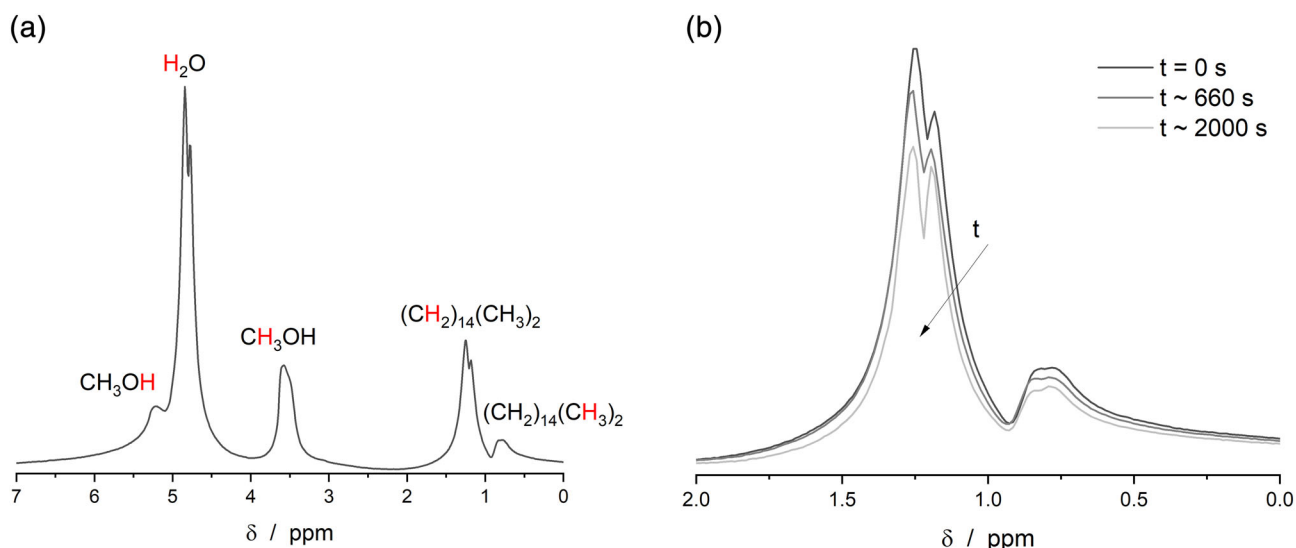
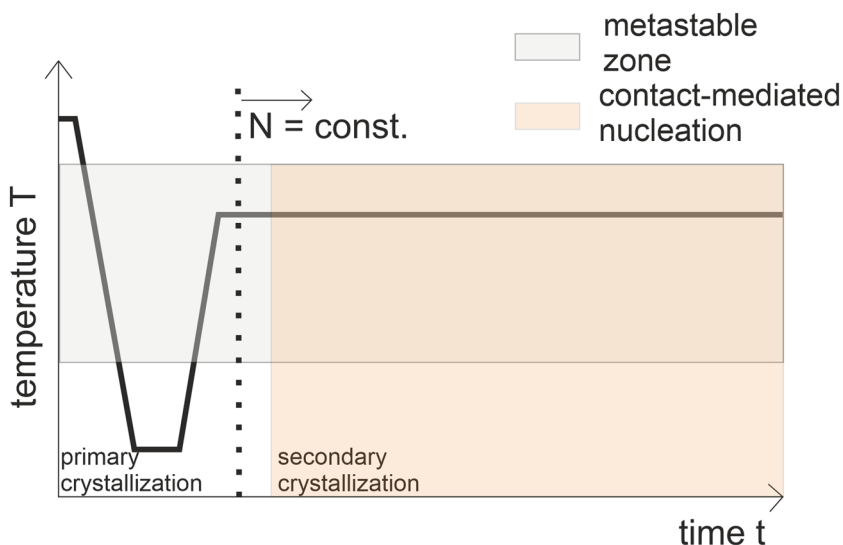


**FIGURE 7** (a)  $^1\text{H}$  spectrum of an emulsion of n-hexadecane-in-water (20 wt-% disperse phase) with the emulsifier Tween<sup>®</sup>20 in the Rheo-NMR cell. In addition to the emulsions' peaks, consisting mainly of residual  $\text{H}_2\text{O}$  (4.6 ppm) and the aliphatic peaks of n-hexadecane (1.26 and 0.78 ppm), the methanol peaks for temperature calibration according to Ammann et al.<sup>[78]</sup> appear at 5.2 and 3.5 ppm. (b) Change of the n-hexadecane NMR signal (liquid) as a function of time during the preceding crystallization in the droplets

After reaching the temperature level for secondary nucleation, a waiting time of 3.5 min was included to ensure good temperature homogeneity and reliability (Figure 2, gray bar). This waiting time guarantees constant temperature during the experiment by means of the thermal properties of GreenTEC (Table 1) and the probe's mixing properties when starting rotation. We double-checked this waiting time for equilibration by observing the methanol in the gap for calculating temperature and rotational profiles.

Only liquid n-hexadecane can be detected by the liquid NMR method described above as the spin-spin relaxation ( $T_2$  relaxation) of crystalline n-hexadecane is too short. Crystalline n-hexadecane, thus, is not visible in the liquid's  $^1\text{H}$  spectra. The signal is consequently

proportional to the number of  $^1\text{H}$  spins in the liquid droplets of the emulsion within the field of view. The fraction of solidified droplets was observed by the decrease of this NMR signal.

#### 4.6 | Data analysis

The fraction of solidified droplets at a given time is defined as the number of crystallized droplets at a given time related to the total number of droplets at the beginning of the experiment. Assuming a known monomodal droplet size distribution, the number density of liquid droplets is proportional to the integral area of the corresponding peaks in the  $^1\text{H}$  spectra (Figure 7).

Figure 7a represents a typical  $^1\text{H}$  spectrum of an emulsion in the TCR at 200 MHz. The chemical shift difference between the two methanol peaks ( $\text{CH}_3$  and OH) reflects the temperature inside the inner cylinder. The calculation was made according to Ammann et al.<sup>[78]</sup> The peaks corresponding to Tween<sup>®</sup>20 are hidden by methanol and n-hexadecane signal contributions. While liquids generally have a low transverse relaxation rate, solids, especially crystalline solids, usually exhibit high transverse relaxation rates. Liquid state NMR spectroscopy can, thus, be used to distinguish the two states of aggregation, liquid and solid, and, hence, allow the fraction of solidified droplets during crystallization to be quantified in situ (Figure 7b). Consequently, the upper and lower integration limits were set to 0.6 and 1.4 ppm, respectively.

## ACKNOWLEDGEMENTS

The authors thank the Bruker BioSpin GmbH,  $\mu$ -imaging group, for their support during this work. The *Deutsche Forschungsgemeinschaft* is thanked for the substantial financial contribution in the form of NMR instrumentation and within the instrumental facility Pro<sup>2</sup>NMR. The authors also would like to acknowledge the workshop employees for their support during the constructions, especially Max Renaud. Special thanks to Philipp Seegert of the Institute for Thermal Process Engineering for providing the specifications of GreenTEC. We also would like to thank Gabriela Saavedra from the Institute of Process Engineering in Life Sciences, Food Process Engineering, for enabling the rheological measurements and Philipp Quarz for conducting the measurements. Open Access funding enabled and organized by Projekt DEAL.

## CONFLICT OF INTEREST

The authors have declared no conflicts of interest.

## ORCID

Gina Kaysan  <https://orcid.org/0000-0002-6773-7803>

Nicolas Schork  <https://orcid.org/0000-0001-5891-8891>

Gisela Guthausen  <https://orcid.org/0000-0002-6444-2663>

Matthias Kind  <https://orcid.org/0000-0002-7203-1776>

## REFERENCES

- [1] A. K. Chesters, *Chem. Eng. Res. Des.* **1991**, *69*, 259.
- [2] E. Dickinson, F.-J. Kruizenga, M. J. W. Povey, M. van der Molen, *Coll. Surf. A Physicochem. Eng. Asp.* **1993**, *81*, 273.
- [3] S. Friberg, K. Larsson, J. Sjoblom, *Food emulsions*, Boca Raton, Florida: CRC Press **2003**.
- [4] V. G. Levich, *Physicochemical hydrodynamics*, Hoboken, New Jersey: Prentice-Hall **1962**.
- [5] P. Walstra, P. E. A. Smulders, *Modern aspects of emulsion science*, London, United Kingdom: The Royal Society of Chemistry **1998** 56.
- [6] J. J. M. Janssen, A. Boon, W. G. M. Agterof, *AIChE J.* **1994**, *40*, 1929.
- [7] R. J. Donnelly, *Phys. Today* **1991**, *44*, 32.
- [8] C. D. Andereck, S. S. Liu, H. L. Swinney, *J. Fluid Mech.* **1986**, *164*, 155.
- [9] J. D. Seymour, B. Manz, P. T. Callaghan, *Phys. Fluids (1994-present)* **1999**, *11*, 1104.
- [10] C. Schmidt, Modern magnetic resonance, in *Part III Materials Science*, (Ed: G. A. Webb), Berlin/Heidelberg, Germany: Springer **2008** 1515.
- [11] P. T. Callaghan, *Rep. Prog. Phys.* **1999**, *62*, 599.
- [12] P. T. Callaghan, *Curr. Opin. Colloid Interface Sci.* **2006**, *11*, 13.
- [13] P. T. Callaghan, *Rheol. Acta* **2008**, *47*, 243.
- [14] P. T. Callaghan, *eMagRes* **2007**.
- [15] P. T. Callaghan, *Principles of nuclear magnetic resonance microscopy*, Oxford, United Kingdom: Oxford University Press on Demand **1993**.
- [16] P. T. Callaghan, *Translational dynamics and magnetic resonance: principles of pulsed gradient spin echo NMR*, Oxford, United Kingdom: Oxford University Press **2011**.
- [17] P. T. Callaghan, A. M. Gil, *Rheol. Acta* **1999**, *38*, 528.
- [18] K. G. Hollingsworth, M. L. Johns, *J. Rheol.* **2004**, *48*, 787.
- [19] K.-F. Ratzsch, C. Friedrich, M. Wilhelm, *J. Rheol.* **2017**, *61*, 905.
- [20] A. Colbourne, T. Blythe, R. Barua, S. Lovett, J. Mitchell, A. Sederman, L. Gladden, *J. Magn. Reson.* **2018**, *286*, 30.
- [21] D. Morimoto, E. Walinda, N. Iwakawa, M. Nishizawa, Y. Kawata, A. Yamamoto, M. Shirakawa, U. Scheler, K. Sugase, *Anal. Chem.* **2017**, *89*, 7286.
- [22] T. Nikolaeva, F. J. Vergeldt, R. Serial, J. A. Dijkstra, P. Venema, A. Voda, J. van Duynhoven, H. Van As, *Anal. Chem.* **2020**, *92*, 4193.
- [23] K. G. Hollingsworth, M. L. Johns, *J. Colloid Interface Sci.* **2006**, *296*, 700.
- [24] M. R. Serial, T. Nikolaeva, F. J. Vergeldt, J. van Duynhoven, H. van As, *Magn. Reson. Chem.* **2019**, *57*, 766.
- [25] G. Ovarlez, S. Rodts, A. Ragouilliaux, P. Coussot, J. Goyon, A. Colin, *Phys. Rev. E* **2008**, *78*, 036307.
- [26] T. Nikolaeva, R. den Adel, R. van der Sman, K. J. A. Martens, H. Van As, A. Voda, J. van Duynhoven, *Langmuir* **2019**, *35*, 2221.
- [27] K. W. Milc, M. R. Serial, J. Philippi, J. A. Dijkstra, J. P. M. van Duynhoven, C. Terenzi, *Magn. Reson. Chem.* **2021**, in press, 1.
- [28] E. Laryea, N. Schuhardt, G. Guthausen, T. Oerther, M. Kind, *Micropor. Mesopor. Mater.* **2018**, *269*, 65.
- [29] G. Kaysan, B. Spiegel, G. Guthausen, M. Kind, *Chem. Eng. Technol.* **2020**, *43*, 1699.
- [30] M. Smoluchowski, *Z. Phys. Chem.* **1918**, *92U*, 129.
- [31] Y. X. Liao, D. Lucas, *Chem. Eng. Sci.* **2010**, *65*, 2851.
- [32] T. Frising, C. Noik, C. Dalmazzone, *J. Dispers. Sci. Technol.* **2006**, *27*, 1035.
- [33] N. Leister, H. P. Karbstein, *Colloids and Interfaces* **2021**, *5*, 21.
- [34] M. L. Taboada, N. Leister, H. P. Karbstein, V. Gaukel, *Chem. Eng.* **2020**, *4*, 47.
- [35] M. Dudek, D. Fernandes, E. H. Hero, G. Oye, *Colloid. Surf. A-Physicochem. Eng. Asp.* **2020**, *586*, 124265.
- [36] T. D. Hodgson, J. C. Lee, *J. Colloid Interface Sci.* **1969**, *30*, 94.

- [37] T. D. Hodgson, D. R. Woods, *J. Colloid Interface Sci.* **1969**, 30, 429.
- [38] B. Derjaguin, L. Landau, *Prog. Surf. Sci.* **1993**, 43, 30.
- [39] E. J. Verwey, J. T. G. Overbeek, *Trans. Faraday Soc.* **1946**, 42, B117.
- [40] E. S. Basheva, P. A. Kralchevsky, K. D. Danov, K. P. Ananthapadmanabhan, A. Lips, *Phys. Chem. Chem. Phys.* **2007**, 9, 5183.
- [41] E. Dickinson, J. G. Ma, M. J. W. Povey, *J. Chem. Soc. Faraday Trans.* **1996**, 92, 1213.
- [42] N. Schork, S. Schuhmann, H. Nirschl, G. Guthausen, *Magn. Reson. Chem.* **2019**, 57, 738.
- [43] S. Schuhmann, J. W. Simkins, N. Schork, S. L. Codd, J. D. Seymour, M. Heijnen, F. Saravia, H. Horn, H. Nirschl, G. Guthausen, *J. Membr. Sci.* **2019**, 570, 472.
- [44] A. Hanlon, S. Gibbs, L. Hall, D. Haycock, W. Frith, S. Ablett, C. Marriott, *Meas. Sci. Technol.* **1998**, 9, 631.
- [45] A. D. Hanlon, S. J. Gibbs, L. D. Hall, D. E. Haycock, W. J. Frith, S. Ablett, *Magn. Reson. Imaging* **1998**, 16, 953.
- [46] A. Gottwald, P. Kuran, U. Scheler, *J. Magn. Reson.* **2003**, 162, 364.
- [47] D. Gabriele, M. Migliori, R. Di Sanzo, C. O. Rossi, S. A. Ruffolo, B. de Cindio, *Food Hydrocoll.* **2009**, 23, 619.
- [48] R. N. Al-kaby, J. S. Jayaratne, T. I. Brox, S. L. Codd, J. D. Seymour, J. R. Brown, *J. Rheol.* **2018**, 62, 1125.
- [49] J. R. Brown, P. T. Callaghan, *Soft Matter* **2011**, 7, 10472.
- [50] T. I. Brox, B. Douglass, P. Galvosas, J. R. Brown, *J. Rheol.* **2016**, 60, 973.
- [51] A. Vallatos, M. C. T. Wilson, A. F. Taylor, M. M. Britton, *EPL (Europhys. Lett.)* **2012**, 99, 68001.
- [52] R. C. Prima, H. L. Swinney, in *Hydrodynamic instabilities and the transition to turbulence*, (Eds: H. L. Swinney, J. P. Gollub), Springer, Berlin Heidelberg, Berlin, Heidelberg **1981** 139.
- [53] K. Kataoka, *Encyclopedia of fluid mechanics* **1986**, 236.
- [54] J. A. Cole, *J. Fluid Mech.* **1976**, 75, 1.
- [55] A. Esser, S. Grossmann, *Phys. Fluids* **1996**, 8, 1814.
- [56] M. J. W. Povey, T. S. Awad, R. Huo, Y. L. Ding, *Eur. J. Lipid Sci. Technol.* **2009**, 111, 236.
- [57] S. Abramov, A. Berndt, K. Georgieva, P. Ruppik, H. P. Schuchmann, *Colloids Surf. A Physicochem. Eng. Asp.* **2017**, 529, 513.
- [58] S. A. Vanapalli, J. N. Coupland, *Food Hydrocoll.* **2001**, 15, 507.
- [59] D. J. McClements, E. Dickinson, M. J. W. Povey, *Chem. Phys. Lett.* **1990**, 172, 449.
- [60] D. J. McClements, S. R. Dungan, *J. Colloid Interface Sci.* **1997**, 186, 17.
- [61] E. M. Mudge, G. Mazzanti, *Cryst. Growth Des.* **2009**, 9, 3111.
- [62] G. Mazzanti, E. M. Mudge, E. Y. Anom, *J Am Oil Chem Soc* **2008**, 85, 405.
- [63] W. J. Howarth, *AIChE J.* **1967**, 13, 1007.
- [64] H. Sovová, *Chem. Eng. Sci.* **1981**, 36, 1567.
- [65] M. Simon, in *Technische Universitaet Kaiserslautern* (Ed.: T. P. Engineering), **2004**.
- [66] G. V. Jeffrey, G. A. Davies, *Recent advances in liquid-liquid extraction*, Amsterdam, Netherlands: Elsevier **1971** 495.
- [67] R. H. Davis, J. A. Schonberg, J. M. Rallison, *Phys. Fluids A: Fluid Dyn.* **1989**, 1, 77.
- [68] G. D. M. MacKay, S. G. Mason, *Can. J. Chem. Eng.* **1963**, 41, 203.
- [69] N. H. Sagert, M. J. Quinn, *Can. J. Chem. Eng.* **1976**, 54, 392.
- [70] F. Lehr, D. Mewes, *Chem. Eng. Sci.* **2001**, 56, 1159.
- [71] F. Lehr, M. Millies, D. Mewes, *AIChE J.* **2002**, 48, 2426.
- [72] L. Doublier, *Int. J. Multiphase Flow* **1991**, 17, 783.
- [73] P. C. Duineveld, T. N. University of Twente, **1994**.
- [74] D. Chappellear, *J. Colloid Sci.* **1961**, 16, 186.
- [75] T. Krebs, K. Schroen, R. Boom, *Soft Matter* **2012**, 8, 10650.
- [76] Q. Zhou, Y. Sun, S. Yi, K. Wang, G. Luo, *Soft Matter* **2016**, 12, 1674.
- [77] B. S. Douglass, R. H. Colby, L. A. Madsen, P. T. Callaghan, *Macromolecules* **2008**, 41, 804.
- [78] C. Ammann, P. Meier, A. E. Merbach, *J. Magn. Reson.* **1982**, 46, 319.

## SUPPORTING INFORMATION

Additional supporting information may be found in the online version of the article at the publisher's website.

**How to cite this article:** G. Kaysan, N. Schork, S. Herberger, G. Guthausen, M. Kind, *Magn Reson Chem* **2021**, 1. <https://doi.org/10.1002/mrc.5228>